Title: Protein detection in blood with single-molecule imaging

Authors: Chih-Ping Mao[1,2]†, Shih-Chin Wang[3]†, Yu-Pin Su[4], Ssu-Hsueh Tseng[5], Liangmei He[6], Annie A. Wu[6], Richard B.S. Roden[5-7], Jie Xiao[3], and Chien-Fu Hung[5-7]*.

Affiliations:

[1]Department of Pathology, Brigham and Women's Hospital, Boston, MA, USA.

[2]Harvard Medical School, Boston, MA, USA.

[3]Department of Biophysics and Biophysical Chemistry, Johns Hopkins University School of Medicine, Baltimore, MD, USA.

[4]Lieber Institute for Brain Development, Baltimore, MD, USA.

[5]Department of Pathology, Johns Hopkins Medical Institutions, Baltimore, MD, USA.

[6]Department of Oncology, Johns Hopkins Medical Institutions, Baltimore, MD, USA.
[7]Department of Gynecology & Obstetrics, Johns Hopkins Medical Institutions, Baltimore MD, USA.

†These authors contributed equally to this work.

*Corresponding author; email: chung2@jhmi.edu (C.F.H.).

Abstract: The ability to identify and characterize individual biomarker protein molecules in patient blood samples could enable diagnosis of diseases at an earlier stage, when treatment is typically more effective. Single-molecule imaging offers a promising approach to accomplish this goal. However, thus far single-molecule imaging methods have only been used to monitor protein molecules in solutions or cell lysates, and have not been translated into the clinical arena. Furthermore, the detection limit of these methods has been confined to the picomolar (10^{-12} M) range. In many diseases, the circulating concentrations of biomarker proteins fall several orders of magnitude below this range. Here we describe Single-Molecule Augmented Capture (SMAC), a single-molecule imaging technique to visualize, quantify, and characterize individual protein molecules of interest down to the subfemtomolar ($<10^{-15}$ M) range, even in complex biologic fluids. We demonstrate SMAC in a wide variety of applications with human blood samples, including the analysis of disease-associated secreted proteins, membrane proteins, and rare intracellular proteins. Using ovarian cancer as a model, a lethal malignancy in which high-grade disease is driven almost universally by alterations in the *TP53* gene and frequently only diagnosed at a late, incurable stage, we found that mutant pattern p53 proteins are released into the blood in patients at an early stage in disease progression. SMAC opens the door to the application of single-molecule imaging in non-invasive disease profiling and allows for the analysis of circulating mutant proteins as a new class of highly specific disease biomarkers. The SMAC platform can be adapted to multiplex or high-throughput formats to characterize heterogeneous biochemical and structural features of circulating proteins-of-interest.

Teaser: A single-molecule imaging approach detects individual disease-specific protein molecules, including mutant intracellular proteins, in blood samples.

Introduction:

Diseased cells release biomarker proteins into the bloodstream (*1*). These proteins can be tissue-specific but normal in structure, contain mutated regions, or carry abnormal secondary modifications. Conventional blood tests, such as the enzyme-linked immunosorbent assay (ELISA), typically cannot discern protein concentrations below the picomolar (pM; 10^{-12} M) range (*1*). The circulating levels of biomarker proteins associated with early stages of common disorders such as cancer or infection frequently fall in the femtomolar (fM; 10^{-15} M) range and below (*2, 3*). Newer methods, including digital ELISA (*4*), DNA biobarcoding (*5*), proximity ligation (*6, 7*), and immuno-PCR (*8, 9*), have been developed to improve the sensitivity of protein assays to the fM range. However, these tests rely on enzymatic amplification and ensemble measurements of the target molecule (*1*). Ensemble methods are limited by detection errors from background or non-specific reagent binding, especially in complex clinical fluids such as blood.

Single-molecule imaging approaches visualize individual protein molecules, providing greater sensitivity, reliability, and depth-of-information than ensemble methods (*10*). The detection limit of single-molecule imaging approaches has thus far reached the pM range in cell lysates (*11, 12*). However, single-molecule imaging of proteins in the blood has not been previously achieved. Here we describe Single-Molecule Augmented Capture (SMAC), a technique that allows quantification of individual protein molecules in the blood down to the sub-fM range. SMAC offers orders of magnitude greater detection sensitivity and specificity than other single-molecule imaging methods, opening up the possibility of, for the first time, quantifying and characterizing disease-associated molecules in patient samples at the single-molecule level. SMAC interrogates images formed by individual target protein molecules within biological samples and uses a fluorescence shape recognition algorithm to correct detection errors derived from non-specific antibody absorption or autofluorescence in complex biological fluids. Thus, true signals are reliably distinguished from false background signals in samples. Here we demonstrate a wide variety of applications of SMAC in blood-based human disease profiling.

Results:

In SMAC, individual proteins-of-interest are continuously pulled down by a capture antibody on a microfluidic device, probed by a fluorophore-labeled detection antibody, and visualized by single-molecule imaging (Fig. 1A). We achieved sub-fM sensitivity by implementing the following strategies (Fig. 1B). First, we created the SMAC chip, a highly efficient target-capture microfluidic device (Fig. 1A). The chip has the following features: (a) it is coated it with a dense layer of multi-valent, biotinylated antibody via a NeutrAvidin linker (*12, 13*), which enhances capture affinity and suppresses non-specific binding; (b) the total capture area of the chip is minimized, which concentrates proteins-of-interest by $>10^4$-fold; and (c) a staggered herringbone micromixer roof (*14*) and oscillating sample flow scheme are incorporated onto the chip, which promote target-antibody collisions (Fig. 1B, S1A, B). Second, we employed a flow cytometry-based antibody screening process to rapidly identify the best capture/detection antibody pairs for target proteins (Fig. S1C, D). Third, we conducted time-stream averaged total internal reflection fluorescence (TIRF) microscopy images to resolve spatially individual fluorescent spots of target protein molecules (Fig. S2A, B; see Methods for details). Time-stream TIRF microscopy

helps overcome diffusive background from autofluorescent substances in test samples and in the microfluidic device itself. These autofluorescent substances dissociate rapidly from the chip surface and photobleach more quickly than fluorophore-labeled detection antibodies. By contrast, detection antibodies specifically bound to target protein molecules remain attached to the chip for a longer time (Fig. S2C). Thus, by time-averaging an imaging stream, SMAC removes autofluorescent background signals while preserving specific signals from detection antibodies (Fig. S2A, B).

Finally, to achieve sub-fM sensitivity with minimal detection errors for proteins of rare occurance in samples, we applied a 'fluorescence shape' recognition algorithm (referred to as shape analysis; see Methods for details). Because NeutrAvidin and the capture antibody are multi-valent (Fig. 1A), fluorophore-labeled detection antibody molecules form clusters around target protein molecules on each NeutrAvidin tetramer, generating fluorescent spots with combinations of size (measured by the σ of the Gaussian fitting of the spot) and intensity (I; measured in number of photons) that are distinct from those of background spots due to diffusive background and non-specifically absorbed detection antibody molecules (Fig. 1C, D). We referred to these combinations of size and intensity as the I-σ shape (Fig. 2A). The I-σ shape reflects the combination of fluorescent signals emitted by specific antibody binding, non-specific antibody binding, and background diffusive autofluorescence and can be deconvoluted into its individual components via shape analysis (Fig. 2A, B). To perform shape analysis, we first represented the I-σ shape of a test sample as a two-dimensional (2D) histogram depicting the absolute number of spots in a set number of I-σ bins (Fig. 2C). We corrected for detection errors by subtracting out the maximum projected number of background reference spots (experimentally derived from a large pool of negative control background samples) from each bin of the test sample I-σ histogram (Fig. 2C). This analysis allowed us to overcome confounding effects of background signals at extremely low target protein concentrations in complex fluids such as blood.

We first validated the design of SMAC using a capture antibody targeting purified GFP. Because GFP is intrinsically fluorescent, we did not use a detection antibody. By applying the shape recognition algorithm, we achieved a limit of detection (LOD) of 61 aM GFP (Fig. 2D, E and Fig. S3A). This detection sensitivity is $>10^4$-fold more sensitive than ELISA and existing single-molecule imaging approaches (*11, 12*) (Fig. S3B). Note that for samples containing proteins of relatively high abundance, such as >10 fM GFP, it is not necessary to use the shape-recognition algorithm. Instead, we measured the overall fluorescence intensity per sample (referred to as integrated intensity analysis) by adjusting the EMCCD (electron-multiplier charge-coupled device) camera gain such that the signal would fall within the linear range of the camera. We then compensated the image signal level using the corresponding EM gain and a standard calibration curve (see Methods for details), allowing us to accurately detect GFP from sub-fM concentrations up to 100 nM in a single sample without the need for dilution (Fig. S3A), which corresponds to a dynamic range of around nine orders of magnitude (compared to approximately two orders of magnitude for ELISA).

Next, we developed SMAC to detect a disease-associated secreted protein, prostate-specific antigen (PSA), as a proof of principle for the application of SMAC to clinical samples (Fig. 3). PSA is a well-established biomarker for prostate cancer (*15-18*). While the normal prostate gland constitutively produces PSA, the expression of this protein is often dysregulated in prostate cancer cells, leading to either elevated or reduced PSA levels in the blood (*15-18*). SMAC could detect purified PSA at an LOD of 648 aM (Fig. 3B, C), 10^5 times below the limit of the

current clinical PSA test (*4*) (Fig. S4B) and is comparable to the reported limit of digital ELISA (*4*). SMAC was able to detect PSA in lysate derived from a single prostate cancer cell titrated into aqueous buffer or human blood (Fig. 3D-F). Furthermore, the SMAC PSA assay achieved a dynamic range of over six orders of magnitude (from 5 fM to >1 nM) (Fig. S4A) compared to two orders of magnitude for the clinical PSA test.

To test if SMAC could monitor circulating PSA in human blood samples, we measured PSA levels in plasma samples from prostate cancer patients (Table S1) as well as from control healthy male and female blood donors (Fig. 3G). We found that in most cases SMAC detected circulating PSA in prostate cancer patients at abnormally high levels (~10-100 pM) compared to baseline PSA levels in healthy male donors (~100 fM) (Fig. 3G). In contrast, conventional ELISA required >10-fold greater plasma volume to detect circulating PSA from prostate cancer patients, and could not detect basal PSA levels in control male blood donors (Fig. S5), which is consistent with prior studies (*4*). We also found that one prostate cancer patient had abnormally low circulating PSA levels (Fig. 3G and Fig. S5); it has been observed that ~10% of prostate cancer patients have very low circulating PSA levels (*19-21*), which correlates with poor prognosis (*22*). These results illustrate the clinical utility of SMAC for established, secreted biomarkers and demonstrate the first single-molecule imaging-based blood test, paving the way to applications of single-molecule imaging in non-invasive profiling of disease-associated proteins.

We next used SMAC to characterize membrane-bound proteins shed into the blood. Programmed death-ligand 1 (PD-L1) (*23*) is a membrane-bound immune checkpoint mediator which inhibits immune responses in a variety of disorders spanning from cancer to infection (*24-26*) and has recently been found in human blood (*27, 28*). PD-L1 antagonists have shown promise in treating chronic virus infection (*29*) as well as multiple cancer types (*30, 31*). A non-invasive approach to predict likelihood of benefit from immune checkpoint blockade could help tailor clinical management to individual patients (*32*). We thus employed SMAC to determine the level of circulating PD-L1 in human blood (Fig. 3H).

We first developed SMAC to detect purified PD-L1 down to aM concentrations (LOD of 607 aM) and with a six-log dynamic range (Fig. 3I, J and Fig. S6A). By comparison, the detection limit of conventional ensemble methods such as ELISA was 10^4-fold higher (~10 pM) and had a two-log dynamic range (Fig. S6B). We next applied SMAC to characterize circulating PD-L1 molecules in patients with a chronic virus infection-induced disease: human papillomavirus (HPV)-associated cervical high-grade squamous intraepithelial lesions (*33*) (HSIL; Table S2). Baseline circulating PD-L1 levels spanned from 50-300 fM in control blood donors (Fig. 3K). By contrast, five of six HSIL patients had blood PD-L1 levels >300 fM, and two of these patients had levels >500 fM (Fig. 3K). By comparison, ELISA could detect circulating PD-L1 in only one of the six HSIL patients (Fig. S7). Circulating PD-L1 was likely increased in a subset of HSIL patients because HPV infection and T cell-mediated local inflammation together induce tissue PD-L1 gene expression (*34*). The heterogeneity in PD-L1 levels is consistent with previously reported percentages of ectopic PD-L1 expression in tissue from HPV-associated lesions (*35, 36*). These results introduce opportunities for single-molecule imaging to investigate the role of circulating immune checkpoint mediators as well as other membrane-tethered proteins in human diseases.

Having demonstrated the detection of extracellular proteins, including secreted and membrane-bound, proteins in blood using SMAC, we next turned to the detection of rare intracellular proteins shed from disease sites into the blood. Current blood tests target extracellular proteins as they are easily accessible (*37*), but many of these proteins are also found in the blood

of healthy people (*38*). In contrast, certain intracellular proteins, in particular those that promote oncogenic transformation—such as mutant or viral oncoproteins, as well as mutant tumor suppressor proteins—are exclusively expressed by diseased cells and hence would be more accurate biomarkers than extracellular proteins. While we and others have observed the release of intracellular proteins from cultured cancer cells (*39*) (Fig. S8A), their presence in blood has not been reported, likely because they lie amidst a plethora of other circulating proteins and are too rare to be quantified by current methods. The idea of identifying circulating intracellular proteins, such as mutant proteins, has remained an elusive goal (*40*).

We first assessed if intracellular proteins from tumor cells are shed into the bloodstream using an animal model in which tumor cells (TC-1 (*41*)) are engineered to express cytoplasmic GFP (cytoGFP) as a prototype intracellular protein (Fig. 4A). We inoculated mice with cytoGFP^{+} tumor cells in either subcutaneous or mucosal (buccal) tissue and were able to detect cytoGFP in the blood of these mice within one week after tumor challenge (Fig. 4B). The concentration of circulating cytoGFP ranged from 1 fM to 1 pM (Fig. 4B), which was in most cases below the ELISA detection limit (Fig. S3B). We then induced mice with spontaneous tumor by electroporating into buccal tissue DNA vectors encoding oncogenes (*42*) (*Ras*^{G12V} and *p53* shRNA) and the intracellular biomarkers cytoGFP (*cyto-gfp*) and luciferase (Fig. S8B). We were able to monitor the accumulation of cytoGFP in serum from these mice (from ~1 fM to ~1 nM), which paralleled tumor burden as measured by buccal luminescence imaging of luciferase activity (Fig. 4C and Fig. S8C). Serum *cyto-gfp* DNA was not detectable by quantitative PCR (qPCR) even when the tumor reached >5 mm diameter (Fig. S8D, E), likely due to the low copy number and labile nature of DNA in the blood (Fig. S8F). These results are consistent with the typically low levels of circulating tumor DNA (ctDNA), especially in early-stage cancer (*43, 44*) (*45-48*). Using SMAC to follow the release of cytoGFP protein over time, we found that circulating cytoGFP levels closely mimicked luminescence imaging of tumor onset and progression (*49*) beyond week two, once the initial circulating cytoGFP peak (due to electroporation-mediated tissue damage) had waned (Fig. 4D and Fig. S9). These results were confirmed by cross-correlation analysis (Fig. 4E). Of note, serum cytoGFP was imperceptible by ELISA even 42 days after tumor was induced (Fig. S10). These results underscore the potential of single-molecule imaging to study fundamental disease processes in animal models, as well as to identify rare intracellular proteins in the blood for early disease detection.

To investigate the release of rare intracellular proteins in a clinically important system, we focused on the transcription factor p53 since it is a well-established tumor suppressor and the most commonly altered protein in human cancers (*50*). We developed SMAC to detect fM levels purified human p53 protein in an aqueous buffer (LOD of 12 fM), ~10^4-fold below the ELISA limit (Fig. 4F, G). In cancer cell lines carrying different mutant p53 variants, we detected substantial levels of p53; by contrast, we detected essentially no p53 in cell lines with wildtype (wt) p53 (Fig. S11A). These results reflect the enhanced stability of mutant p53 relative to wt p53, as the latter undergoes rapid degradation by proteasomes (*51, 52*). Note that we used anti-p53 antibodies that theoretically recognize total p53, including wildtype and mutant variants. However, because only the mutant form of p53 is detectable in cell lines, in subsequent experiments we interpreted the presence of p53 in samples as 'mutant pattern' p53. We were able to observe mutant p53 release into the extracellular milieu from as few as 300 human ovarian cancer cells (OVCAR3) cultured overnight (Fig. S11B).

We optimized SMAC with shape analysis to correct background signals for p53 spiked into serum (Fig. S11C). To characterize mutant p53 proteins shed into the bloodstream in an animal model, we induced tumor formation in mice by co-delivery of DNA encoding human mutant $p53^{R175H}$, Ras^{G12V}, and luciferase into the buccal mucosa using electroporation. We measured serum mutant p53 proteins in these mice over time by SMAC with shape analysis. Circulating mutant p53 levels rose in parallel with tumor progression (from ~75 fM two weeks after tumor onset to ~2 pM after two months), even in the case of tumor metastasis, as assessed by luminescence imaging (Fig. 4H, I and Fig. S12A, B).

We next utilized SMAC to identify mutant p53 proteins in the blood of patients with high-grade ovarian cancer (HGOC; Table S3) (Fig. 5A), since the tumor from >96% of HGOC patients contains mutations in the *TP53* gene (*53*). Using normal human plasma spiked with purified p53, we verified that SMAC with shape analysis maintained fM baseline sensitivity (LOD of 35 fM) for p53 in human blood yet corrected >96% of background errors (Fig. 5B, C and Fig. S13). We detected mutant pattern p53 molecules in ~60% of plasma samples from HGOC patients with disseminated (FIGO stage III) disease (ranging from <10 fM to 1 pM) but in none of the samples from age-matched control female blood donors (Fig. 5D). We reasoned that for patients with undetectable circulating p53, host autoantibodies may have depleted p53 proteins (*54*) or blocked their capture (Fig. 5A). We therefore developed SMAC to identify autoantibodies against p53. SMAC exhibited $>10^3$-fold greater sensitivity than existing assays and could detect autoantibodies in picoliter (10^{-12} l) volumes of human blood (Fig. 5E, F). Using SMAC, we measured abundant amounts of plasma anti-p53 autoantibodies in 43% of the cohort of HGOC patients (~10^3-fold in excess of circulating mutant p53 levels) but not from any healthy donors (Fig. 5G). Interestingly, the presence of circulating mutant p53 and its autoantibodies appeared anti-correlated (Fig. 5H), suggesting that host immune responses might have cleared mutant tumor antigens from the blood or that autoantibodies disrupted capture of p53 (*55, 56*). Altogether, SMAC detected circulating p53 protein or abundant anti-p53 autoantibodies in 86% of HGOC patients and in no healthy subjects (Fig. 5H).

We next characterized the levels of circulating mutant p53 and anti-p53 antibodies in an independent validation cohort of ovarian cancer patients with well-defined clinical information and p53 mutation status presenting at various pathologic stages, including early-stage (FIGO stage I and II) disease, either pre- or post-surgical resection. These samples were from the same cohort of patients included in the recent study describing the CancerSEEK technique by Vogelstein and coworkers (*45*). Of note, detection of ovarian cancer at an early stage, when surgical resection may be curative, remains a critical challenge in the field, as less than 20% of ovarian cancer cases are identified at stage I or II (*57*). Among ovarian cancer patients with stage III disease—all of whom carried mutant p53 within the tumor (Table S4)—79% (15 of 19) had either circulating mutant p53 (8 of 19) or anti-p53 autoantibodies (8 of 19) prior to surgical resection (Fig. 5I and Fig. S14). Only one patient had both mutant p53 and anti-p53 autoantibodies within the blood. Together, these results suggest that the presence of circulating mutant p53 and its autoantibodies is anti-correlated. Two of the four patients without circulating mutant p53 or anti-p53 autoantibodies had non-serous ovarian cancer (carcinosarcoma and undifferentiated carcinoma) (Table S4). The role of p53 alterations as a driver of serous ovarian cancer has been well-established (*53*), but its role in other histologic types of ovarian cancer remains unclear. Among stage III ovarian cancer patients previously treated by surgical resection, only 25% (2 of 8) had mutant p53 in the plasma (Fig. 5I and Fig. S15), suggesting that circulating mutant p53 levels serve as an index of tumor progression following therapy.

Included in the validation cohort were seven ovarian cancer patients with early-stage (stage I and II) disease (Table S5). We identified circulating mutant p53 protein in four of these patients (Fig. 5J), all of whom also carried corresponding genetic alterations in *TP53* within their tumors (Table S4). However, the three patients without circulating mutant p53 protein had tumors that lacked *TP53* alterations (Table S4). Interestingly, all early-stage ovarian cancer patients with p53-mutant tumors displayed circulating mutant p53 but not anti-p53 autoantibodies, suggesting that autoantibodies have not yet formed against p53 in patients with early-stage disease. Together, these data indicate that intracellular mutant driver proteins, such as p53, are shed into the bloodstream early on in tumorigenesis, and the analysis of these proteins by single-molecule imaging, in conjunction with tissue-specific biomarkers, may facilitate earlier, more accurate detection and diagnosis of disease, when surgical resection would have more clinical benefit.

The potential applications of ultra-sensitive single-molecule protein imaging extend beyond quantification of target proteins. In fact, SMAC can be used to investigate biochemical properties (e.g., secondary modifications, structural changes, aggregation status) of individual proteins-of-interest within a population, as well as unique combinations of proteins in macromolecular complexes. Because disease-associated proteins often differ between patients and healthy people not only in their total amount but also in their biochemical features, SMAC adds a new dimension to the information obtainable from existing methods.

To explore this avenue, we developed SMAC to investigate the aggregation status of p53 complexes in test samples. Of note, certain conformational mutants of p53 have been shown to self-assemble into high-order complexes within tumor cells, and these mutants have been correlated with aggressive disease (*58*). Thus, the ability to identify these conformational p53 mutants could improve disease detection and management. To test the idea that SMAC could distinguish between conformational p53 mutants, we generated p53 mutants which have been reported to self-assemble into large complexes ($p53^{R175H}$) or remain as monomers ($p53^{L344P}$) (Fig. S15A). We fused these mutants to the GFP reporter protein. We then added the recombinant mutant or wildtype p53 into buffer at different concentrations and examined them by SMAC. We found that the p53 conformational mutants produced different combinations of the number and intensities of fluorescent spots despite equal protein amounts (Fig. S15B, C). For example, at the same total p53 concentration, $p53^{L344P}$ had a large number of low intensity spots; by contrast, $p53^{R175H}$ had fewer spots, but these spots were of high intensity (Fig. S15B, C).

We characterized the intensity distributions of the fluorescent spots and measured the percentage of aggregates (defined as spots greater than or equal to tetramer) in each group of conformational mutants (Fig. S15D-F). At the same p53 concentration, $p53^{R175H}$ had the largest percentage of aggregates, followed by the wildtype group and then $p53^{L344P}$ (Fig. S15E). Also, the relationship between the percentage of aggregates and fluorescent spot number was different among each group of conformational mutants (Fig. S15F). We found that the aggregation-prone $p53^{R175H}$ mutant had the widest intensity distribution of fluorescent spots, followed by wildtype p53, and then the monomeric $p53^{L344P}$ mutant for a given spot number (Fig. S15D). To quantify these data, we calculated the Fano factor of fluorescent p53 spots (defined as the variance in intensity divided by the mean intensity; see Methods for details) as a relative index of the aggregation status (and therefore the likely mutation status). The $p53^{R175H}$ mutant had the greatest change in Fano factor per unit change in spot number, followed by wildtype p53 and then the $p53^{L344P}$ mutant (Fig. S15G). These data indicate that SMAC can reveal conformational properties of disease-associated proteins and open up the possibility of using single-molecule imaging to

investigate the structural properties of mutant p53, as well as other disease-associated proteins, in clinical samples.

Discussion:

In this study, we describe a technology, SMAC, that improves the sensitivity of single-molecule imaging techniques by over 1,000-fold and, for the first time, enables direct single-molecule imaging of disease-related protein biomarkers in clinical samples. SMAC integrates an efficient microfluidic capture platform with single-molecule timestream fluorescence microscopy to achieve this unprecedented sensitivity. Moreover, we developed an error correction algorithm which minimizes background detection noise due to sample autofluorescence or non-specific detection antibody binding. Of note, these sources of noise pose a critical obstacle in the protein diagnostics field and determine the ultimate level of sensitivity that can be reached. We report detection limits in the sub-fM range for multiple clinically important biomarkers, which exceeds the limits of currently employed diagnostic tests by several orders of magnitude. In addition, SMAC attains a dynamic range of at least six orders of magnitude, which is exponentially greater than most existing assays. Thus, we envision SMAC as a valuable platform technology which will advance the field of non-invasive diagnostics.

Indeed, we demonstrate a variety of applications of SMAC to interrogate clinically important biomarkers, such as PSA or PD-L1, in patient blood samples. Perhaps more significantly, we also use SMAC to identify novel classes of biomarkers, including intracellular mutant proteins. Of note, in the cancer diagnostics field, virtually all currently assessed biomarkers are extracellular proteins, and the presence of intracellular biomarkers (such as mutant transcription factors or dysfunctional signaling complexes) remains almost entirely unexplored. Although rare, these mutant or dysregulated intracellular biomarkers likely represent much more specific disease biomarkers because they play crucial function roles in disease pathogenesis. We found that intracellular tumor-derived proteins are released into the blood at an early stage in cancer formation and accumulate in the systemic circulation as the disease progresses. Therefore, these biomarkers may be useful both for early detection and for disease monitoring. The mechanisms by which intracellular proteins are shed from tumor cells into the blood remain unknown, but may be related to a combination of accelerated cellular turnover (*59-63*) and active secretion, as has been documented in *in vitro* studies (*39*). We have conducted preliminary experiments which suggest that oncogenic signaling pathways, including the RAS/RAF/MAPK axis, may contribute to active secretion of intracellular proteins (data not shown).

We discovered that a key mutant transcription factor, p53, is found in the blood of ovarian cancer patients with as early as stage I disease. Of note, detection of circulating p53 coincides with the presence of mutant p53 DNA within tumor tissue, as assessed by next-generation sequencing. Indeed, we identified circulating p53 in stage I/II ovarian cancer patients with corresponding alterations in p53 DNA, but not in patients with wildtype p53. Furthermore, interestingly, we observed that, in general, no circulating p53 was identified in patients with stage III/IV disease who produced anti-p53 antibodies, hinting that these antibodies may clear mutant p53 from the bloodstream.

In summary, our results illustrate broad applications of single-molecule imaging to characterize disease-associated secreted, membrane, and intracellular proteins in the blood, opening new avenues to detect, diagnose, and study disease. We are in the process of converting the SMAC technology into a platform that can be broadly applied in clinical practice. To achieve this, we are developing an integrated device that combines the microfluidic handling, single-molecule imaging, and data analysis components of SMAC. The total run-time of the SMAC assay

is approximately 4 hours, including target protein capture, detection antibody incubation, and single-molecule imaging, which is in-line with the time required for existing protein detection methods. Furthermore, while we have found that the sensitivity of SMAC correlates with affinity of the capture/detection antibodies employed, detection limits in the fM and sub-fM range are attained with antibodies with dissociation constants (K_D) ~10 nM or lower, which can be achieved for the vast majority of target proteins with modern antibody production technologies. Thus, we believe the SMAC platform can be readily adapted for disease detection, diagnosis, and monitoring in the clinical setting.

While it introduces single-molecule imaging into the clinical arena and serves as a powerful tool for disease profiling, there are limitations of the SMAC system in its present form. First, the TIRF microscope imaging is performed sequentially, with a total acquisition time of approximately 5 minutes per sample. Thus, the scale at which samples can be run is currently limited. Second, for target proteins that are disease-specific and absent in control samples (such as mutant tumor proteins), control plasma from healthy blood donors can be used in the data analysis algorithm to normalize for background fluorescence in the blood (such as from substances that cause autofluorescence or non-specific detection antibody binding). However, for target proteins that are also present to varying degree in control samples, such as tumor-associated proteins, buffer solution (rather than plasma) must be used as a negative control. For these types of target proteins, the analysis algorithm unable to separate true signal from background in plasma.

Altogether, the insight gained from SMAC may shed light on pathologic processes, such as dysfunctional signaling pathways, gene expression networks, or immune responses unfolding within disease and point to effective therapies. The platform described here may be adapted to investigate unique biochemical, conformational, and structural features of proteins-of-interest in the blood. The design of SMAC can also be readily converted into multiplex and high-throughput formats to enable large-scale, single-molecule profiling of proteins in human disease.

Materials and Methods:

Materials

Polydimethylsiloxane (PDMS) elastomer for synthesis of the single-molecule microfluidic capture device was purchased from Dow Corning. 22×22 mm borosilicate cover glass (Thermo Fisher Scientific) served as the substrate for the capture surface. Surface passivation required the following reagents: *N*-(2-aminoethyl)-3-aminopropyltrimethoxysilane (United Chemical Technologies), Alconox (Alconox, Inc.), methanol (Fisher Scientific), acetic acid (Sigma-Aldrich), sodium bicarbonate (Sigma-Aldrich), biotin-mPEG-succinimidyl valerate MW 5,000 (biotin-mPEG-SVA) (Laysan Bio), and mPEG-succinimidyl valerate MW 5,000 (mPEG-SVA) (Laysan Bio). For GFP detection, biotinylated anti-GFP antibodies (clone RQ2, MBL) were used. For PSA detection, biotinylated (BAF1344, R&D Systems) and Alexa Fluor 488-conjugated (clone 8301, Medix Biochemica) anti-human PSA antibodies were used. For PD-L1 detection, biotinylated (BAF156, R&D Systems) and Alexa Fluor 555-conjugated (clone 28-8, Abcam) anti-human PD-L1 antibodies were used. For human p53 detection, biotinylated (BAF1355, R&D Systems) and Alexa Fluor 555-conjugated (clone E47, Abcam) anti-human p53 antibodies were used. For human p53 detection in mice, biotinylated (BAF1355) and Alexa Fluor 488-conjugated (FL-393, Santa Cruz Biotechnology) antibodies were used. For detection of human anti-p53 autoantibodies, Alexa Fluor 555-conjugated anti-human IgG (H+L) cross-absorbed secondary antibodies (A-21433; Thermo Fisher Scientific) were used. Purified recombinant GFP (Cell Biolabs), human PSA (R&D Systems), human PD-L1 (R&D Systems), and human p53 (R&D Systems) were used to generate standard curves. BSA (New England BioLabs) and polyoxytheylene (20) sorbitan monolaurate (Tween-20; Thermo Fisher Scientific) were used for sample wash and dilution in single-molecule experiments. ELISA for GFP, PSA, PD-L1, p53, and anti-p53 autoantibodies was performed with GFP ELISA Kit (Cell Biolabs), PSA Quantikine ELISA Kit (R&D), PD-L1 Quantikine ELISA Kit (R&D), p53 SimpleStep ELISA Kit (Abcam), and Mesacup Anti-p53 Test (MBL International), respectively, according to manufacturer instructions.

Antibody conjugation

Antibodies were labeled with biotin or organic fluorophores via NHS-reactive ester. For biotin conjugation, antibodies (0.1-1 mg/ml) were incubated with 50-fold molar excess of NHS-LC-biotin (Thermo Fisher Scientific) for 30-60 min and then isolated on 7 kD gel filtration columns (Thermo Fisher Scientific). For dye conjugation, antibodies were pre-captured on protein G magnetic beads (Thermo Fisher Scientific) and incubated with 10-fold molar excess of Alexa Fluor dye-NHS (Thermo Fisher Scientific) for 30-60 min. Free dye was washed out, and antibodies were further purified on 7 kD gel filtration columns. Degree of labeling and concentration of antibodies were measured by spectrophotometry.

Pairwise antibody screening

To select the best pair of capture and detection antibodies recognizing proteins-of-interest, candidate antibodies were each labeled with biotin or organic dye as described above. Pairwise combinations of these candidate antibodies were then evaluated by flow cytometry on microbeads. Biotinylated capture antibodies (1 μg) were incubated with streptavidin M-280 magnetic Dynabeads (10^5 beads per sample; Thermo Fisher Scientific) for 30 min. The beads were washed with PBS and incubated with or without purified target proteins for 30 min. Beads were washed with PBS and incubated with different dye-labeled detection antibodies (1 μg) for 30 min. These

procedures were carried out in 50 μl total volume at 25°C with constant mixing. Beads were then washed, resuspended in PBS (500 μl), and interrogated by flow cytometry on a FACSCalibur device (BD Biosciences). The capture/detection efficiency for each pair of antibodies was calculated based on the shift in mean fluorescence intensity in the presence versus absence of target proteins. Antibodies that yielded the greatest shift were considered to have superior performance.

Purification of recombinant human p53

Human p53 was generated in-house for anti-p53 autoantibody detection experiments. Plasmid encoding human p53 (hp53; Addgene) was inserted into the pET28a bacterial expression vector. *hp53* was first amplified by PCR with the following primer set: 5' AAAGGATCCATGGAGGAGCCGCAGTCAGA 3' and 5' AAAGAATTCCAGGTGGCTGGAGTGAGCCC 3'. The PCR product was cloned into the BamHI/EcoRI sites of the pET28a vector to create pET28a-hp53. This plasmid was transformed into *E. coli* BL21 competent cells (Novagen). Protein expression was induced with 1 mM isopropyl-b-D-thiogalactopyranoside (IPTG) at 37°C for 5 hr. Bacteria were lysed, and the soluble fraction was collected. Recombinant protein was purified by affinity chromatography on Ni-NTA agarose (Qiagen) per manufacturer instructions. Purified p53 was verified by 10-15% gradient sodium dodecyl sulfate polyacrylamide gel electrophoresis (Bio-Rad) and Coomassie Brilliant Blue (Thermo Fisher Scientific) staining, dialyzed with PBS, and stored at -80°C in PBS containing 20% glycerol.

Cells

TC-1 cells were previously generated in our laboratory and have been reported(*41*). For experiments involving cytoGFP, TC-1 cells were retrovirally transduced with a *cyto-gfp* DNA expression cassette. LnCaP human prostate cancer cells were obtained from ATCC. Human cells without p53 (BHK21) and with mutant p53 (CFPAC-1 (C242R), OVCAR3 (R248Q), and TOV-112D (R175H)), cells with wildtype p53 (MCF-7, MCF-10), and HEK 293T cells were from ATCC. Cells were cultured in RPMI-1640 medium or DMEM (Thermo Fisher Scientific) with 10% FBS in the absence of phenol red and maintained under 5% CO_2 atmosphere. Lysate was prepared using commercial lysis buffer (Abcam). Briefly, cells were harvested and resuspended in lysis buffer at a stock concentration of 10^4 cells per μl. The resultant solution was centrifuged at 10,000×*g* at 4°C for 10 min. Target protein concentration in the stock lysate was determined by ELISA. For single-molecule imaging experiments, lysate was diluted 10^3-10^5× in 'SMAC buffer' (10 mM Tris-HCl pH 8.0, 50 mM NaCl, 0.05% Tween-20) with 0.1 mg/ml BSA. For experiments involving supernatant, conditioned medium was collected from cells cultured for 12-24 hr and centrifuged at 1,000×*g* for 5 min. The resultant supernatant was passed through 0.22-μm filters to further remove debris. The number of viable cells was determined using an automated cytometer (Countess II, Invitrogen) with trypan blue dye exclusion.

ELISA

Enzyme-linked immunosorbent assay (ELISA) was performed according to the manufacturer's instructions. Briefly, plasma or cell lysate (50 μl) was added to sample diluent (50 μl). The mixtures were then added to antibody pre-coated plates and incubated at room temperature for 2 hours. The plates were washed with PBS containing 0.05% Tween-20, and HRP-conjugated antibodies were then added to the plate and incubated at room temperature for 2 hours. The plates were washed as above and then developed with TMB substrate solution. The reaction was

terminated with stop solution containing 1 M phosphoric acid. The signals in the plates were measured at 450 nm wavelength using a microplate reader (Bio-Rad).

Mice

6- to 8-week old female C57BL/6 and immune-deficient athymic nude (*Foxn1*$^{-/-}$) mice were obtained from the National Cancer Institute. C57BL/6 mice were used for experiments in which tumor cells were directly inoculated. *Foxn1*$^{-/-}$ transgenic mice were used for experiments in which a spontaneous tumor was induced by oncogene delivery. All animal procedures complied with protocols approved by the Johns Hopkins Institutional Animal Care and Use Committee and with recommendations for the proper use and care of laboratory mice.

Transplanted tumor challenge

C57BL/6 mice were injected with cytoGFP-transduced TC-1 cells (10^5 cells per animal) in the flank (subcutaneous tissue) or buccal mucosa. At one week after tumor challenge, whole blood was collected from the tail vein and processed into serum for downstream experiments. Tumor growth was monitored by visual inspection, palpation, and digital caliper measurement.

Spontaneous tumor induction

Foxn1$^{-/-}$ transgenic mice were injected in the buccal mucosa with a plasmid DNA cocktail encoding (1) mutant Ras^{G12V}, (2) SB13 transposase, (3) firefly luciferase, and (4) either anti-p53 shRNA carrying a GFP expression cassette or mutant human p53^{R175H} (10 μg of each plasmid diluted with PBS to 30 μl total volume); plasmids were acquired from Addgene. Immediately afterward, mice received electroporation (eight pulses of 72 V, 50 ms duration, and 200 ms interval) at the injection site with an ECM830 device (BTX). Tumor burden was monitored over time by whole body luminescence imaging of luciferase activity with an IVIS Spectrum device (PerkinElmer) following intraperitoneal D-luciferin (Promega) injection. At defined time points after tumor induction, whole blood was collected from the tail vein and processed into serum for downstream experiments.

Cross-correlation analysis

To characterize the time relationship between tumor progression and fluctuations in circulating target protein levels in mice, the covariance was calculated between time series of error-corrected single-molecule serum target counts and luminescence photon counts. The covariance coefficient was computed via the 'xcov' function in Matlab (MathWorks). The time lag was narrowed down to five units, with each lag unit corresponding to approximately five days.

Human subjects

Blood samples were obtained from volunteer patients previously diagnosed with prostate adenocarcinoma (n = 5), high-grade cervical intraepithelial lesions (n = 6), and ovarian cancer (n = 48) who underwent clinical evaluation and management at the Johns Hopkins Hospital, Baltimore, MD, USA. Descriptions of the clinical characteristics of individual patients are provided in Tables 1-3. Human studies were approved by the Johns Hopkins University Institutional Review Board (protocol number: IRB00169055). Plasma from healthy human volunteers was acquired from Innovative Research, processed from whole blood in dipotassium ethylenediaminetetraacetic acid (K2-EDTA; BD Biosciences).

Human plasma preparation

Whole blood was drawn from test subjects and anticoagulated with K2-EDTA. Samples were processed within 4 hr after collection. Blood samples were diluted with an equal volume of 1× HBSS (Corning) and added slowly on top of Lymphoprep solution (15 ml; Stem Cell Technologies) in 50-ml conical tubes (Corning). Samples were centrifuged at 1,200×*g* for 10 min at room temperature. The top layer was harvested as plasma and stored at -80°C.

Single-molecule capture surface passivation

Borosilicate coverslips of 130-170 μm thickness and 22×22 mm area served as the substrate for the capture surface. Coverslips were first cleaned in 1% Alconox with sonication for 10 min, washed with Milli-Q water (Millipore) for 10 min, and dried with filtered air. Coverslips were exposed to high power atmospheric plasma using a PE25-JW device (Plasma Etch) for 5 min for surface cleaning and activation, and then immediately dipped in methanol containing 1% *N*-(2-aminoethyl)-3-aminopropyltrimethoxysilane and 5% glacial acetic acid. Coverslips were washed thoroughly with methanol and Milli-Q water, and then dried with filtered air. Coverslips were conjugated with biotin-mPEG-SVA (0.3 mg) in 10 mM sodium bicarbonate (pH 8.5) for 6 hr in a sandwich arrangement. The glass surface was then conjugated with a mixture of biotin-mPEG-SVA (0.3 mg) and PEG-mSVA (16 mg, 1:50 mass ratio) for 12 hr in a sandwich arrangment. After passivation, coverslips were washed with Milli-Q water and dried as described above. Coverslips were transferred to a clean container, vacuumed, flushed with pure nitrogen, sealed with paraffin film, and stored at -20°C. Tween-20 was added into SMAC buffers during downstream experiments to further block the surface.

Microfabrication of the SMAC chip enclosure

A master template for the device enclosure was synthesized by photolithography. Briefly, a silicon wafer was rinsed with acetone and isopropanol and then dehydrated at 200°C for 15 min. The wafer was exposed to high power oxygen plasma (100 W for 3 min at 300-500 mTorr oxygen pressure) using a PE II-A apparatus (Technics) to promote photoresist adhesion. SU-8 photoresist 2050 (MicroChem) was spin-coated onto the wafer to 100 μm thickness. The wafer was then soft-baked (65°C/95°C) for 5 min and exposed to UV light in an EVG620 mask aligner (EVG) loaded with a mask printed at 32,512 DPI resolution (Fineline Imaging). The wafer was then hard-baked (65°C/95°C) for 15 min. The first layer of the microfluidic device consisted of the main channel with side boxes while the second layer contained arrays of staggered herringbone grooves. After all layers of photoresist were deposited, the wafer was developed under ultrasonic agitation to yield a master template for synthesis of the silicone elastomer enclosure. To produce this enclosure, PDMS elastomer was mixed with curing agent in a 10:1 ratio (by weight), poured onto the patterned wafer, degassed, and incubated at 80°C overnight. The PDMS was then removed from the master, cut into individual devices, and bored with inlet/outlet tubing holes (750 μm diameter). The devices were washed in an ultrasonic bath with isopropanol for 20 min and then with Milli-Q water for 5 min. Devices were dried with filtered air.

Assembly of the SMAC chip

Prior to assembly, the uncoated side of the borosilicate coverslip was taped to an alignment guide imprinted with a two-dimensional replica of the flow channel. An elastomer cover microfabricated with μm-precision by photolithography to match the exact size and shape of the flow channel was then placed on the coated side of the coverslip at the position of the channel

replica on the alignment guide. This cover protects the PEG/biotin-PEG layer from oxygen plasma bombardment during the assembly procedure. The coated coverslip surface with elastomer cover and PDMS enclosure were placed inside a PE-25JW plasma etcher and treated with oxygen plasma for 30 sec at 40 W RF power under 100 mTorr oxygen atmosphere. The elastomer cover was removed, and PDMS devices were then sealed to the coated side of the coverslip under a stereomicroscope with the alignment guide as a reference for the channel position. The microfluidic chip was incubated at 80°C for 3 min to drive the bonding to completion.

Preparation of the SMAC chip

Reagent introduction, removal, and wash steps were performed in parallel under automated flow actuated by a multi-channel peristaltic pump (Ismatec). The SMAC chip was connected to inlet and outlet non-shrinkable Teflon tubing (internal diameter 0.015 in; Weico Wire and Cable) and infused with 'SMAC buffer': 10 mM Tris-HCl pH 8.0, 50 mM NaCl, and 0.05% Tween-20. The inclusion of Tween-20 in the SMAC buffer further blocked non-specific protein absorption to the PDMS chamber and the capture surface. To evacuate any air trapped inside the PDMS channel, the chip was immediately degassed under vacuum for 1 min. The chip was equilibrated with SMAC buffer at 50 µl/min flow rate for 10 min. The chip was then incubated with NeutrAvidin (20 µl; 0.1 mg/ml; Thermo Fisher Scientific) in SMAC buffer for 10 min. The chip was washed with SMAC buffer (1 ml) at 500 µl/min and incubated for 30 min with biotinylated antibodies (2 µl; 0.1-1 mg/ml) in SMAC buffer with 0.1 mg/ml BSA ($SMAC^{BSA}$ buffer). The chip was then washed with $SMAC^{BSA}$ buffer (1 ml) at 500 µl/min and ready for sample circulation.

Sample circulation in the SMAC chip

Continuous oscillating flow was actuated by a multi-channel bidirectional AL-8000 syringe pump (World Precision Instruments) connected to the SMAC chip via a 26-gauge 1-cc syringe (BD Biosciences). The chip was connected at the other tubing port to the sample prepared in $SMAC^{BSA}$ buffer. For oscillating flow, the blood sample was diluted to anywhere between 2% to 50% with $SMAC^{BSA}$ buffer in 200-500 µl final volume. Note that although we used 200-500 µl final sample volumes in this study, the SMAC system can actually accommodate volumes up to 10 ml without significant loss in sensitivity because of its oscillating flow scheme and efficient target capture. By contrast, most other methods are unable to reliably detect proteins in sample volumes much greater than 100 µl. The syringe pump was programmed to carry out repeated infusion/withdrawal cycles at 500 µl/min for 2-4 hr. Afterward, the chip was washed with $SMAC^{BSA}$ buffer (1 ml) at 500 µl/min, incubated with fluorophore-labeled detection antibodies (1-10 nM) for 30 min, and then washed again with SMAC buffer (1 ml) at 500 µl/min. For circulation of clinical plasma samples, the prostate cancer patient samples were diluted 50 times. HSIL patient samples were diluted two times. HGSOC patient samples were diluted two times for p53 detection and 10^3-10^6 times for anti-p53 autoantibody detection. For circulation of mouse samples, serum was diluted four times. All dilutions were carried out in $SMAC^{BSA}$ buffer. For experiments involving human samples, ~10^4-fold excess IgG matched to the isotypes of the capture and detection antibodies was further added to reduce non-specific binding.

Single-molecule TIRF microscopy

An objective-based TIRF setup was employed with a PlanApo 60× oil objective (Olympus) of high numerical aperture (1.45). While acquiring data, we also used a 1.6× field lens to capture single-molecule images at 96× total magnification. The incident laser angle was adjusted to full

TIRF mode with a prism. Flow channels in the SMAC chip were identified under brightfield illumination. An imaging region of 15×15 μm^2 was then set. An electron multiplying charge-coupled device camera (Andor) was programmed to capture a consecutive time stream of 500 frames with 50 ms exposure time under continuous laser excitation of 40-140 W/cm^2. Immediately prior to imaging, we measured laser power and TIRF angles to confirm that they were consistent. After imaging each region, the stage was displaced 80 µm down the length of the channel, and imaging was performed again as above. This process was repeated until at least 10 view fields were recorded per sample. Data were acquired with custom journals written in MetaMorph software (Molecular Devices).

Integrated intensity analysis. This method was used to quantify relatively abundant proteins-of-interest (e.g. >10 fM) across a wide dynamic range (6-9 logs). Single-molecule TIRF data were first recorded using a camera EM gain setting of 300. The EM gain of the camera (i.e., 300, 10, or 1) was chosen according to predefined criteria based on the standard curve for that protein. These criteria were set such that the florescence for the sample would fall within the linear range of the standard curve for that EM gain setting.

Single-molecule shape analysis

This method was used for rare proteins-of-interest to correct detection errors due to diffusive background and non-specific binding. The first 50-100 frames of each TIRF image were initially averaged to reduce background fluorescence from compounds arbitrarily deposited on the microfluidic capture chip, as these compounds bind weakly and rapidly dissociate from the chip. We measured the total number of fluorescent spots over 10 view fields in order to maximize sensitivity for rare target proteins. Single-molecule data were interpreted with the ThunderSTORM plug-in in ImageJ software (*64*). In ThunderSTORM, a wavelet filter was applied to remove noise and automatically identify fluorescent spots at a constant low threshold for each sample independent of the target protein. A low threshold setting was chosen in order to ensure that all potential target spots were selected regardless of variations in laser illumination intensity.

The major principle behind shape analysis is that, because target proteins are pulled down as complexes by multivalent antibodies via NeutrAvidin adapters, the shape of fluorescent spots, each represented in coordinates of (I; measured in number of photons) and diffraction-limited spot size (measured by the σ of the Gaussian fitting of the spot), was non-identical between real signals and false signals from diffusive and non-specifically absorbed antibody molecules. Therefore, a raw SMAC image can be deconvoluted into its real and false (i.e. background) components. To do so, we converted each selected spot in the raw SMAC image into an I-σ coordinate and sorted each spot into its respective bin in a 2D I-σ histogram. Note that each bin i of this histogram contains both real and false spots, adding up to a total of T_i spots. The next step in the analysis is to determine the number of false spots in each bin. For each target protein under different conditions, we performed SMAC on control samples lacking the target protein. For experiments involving aqueous buffer and cell supernatant, $SMAC^{BSA}$ buffer and culture medium, respectively, were used as reference samples. For animal experiments, serum from naïve mice was used as reference samples. For experiments involving human blood, plasma from multiple independent healthy blood donors was used as reference samples.

The identified spots in these control images were also sorted into bins in a 2D I-σ histogram. Note that each bin of this reference histogram contains only false spots. By running this assay and analysis procedure on a large set of reference samples (e.g. buffer only or blood samples from many individual healthy donors), the mean (R_i^{μ}) and standard deviation (R_i^{SD}) of the number

of spots in each bin was calculated. To correct detection errors and compute the number of real spots (C_i^{μ}) for each bin, the following formula was used: $C_i^{\mu} = T_i - \left(R_i^{\mu} + n \times R_i^{\mathrm{SD}}\right)$, where n can be adjusted the control the maximum number of projected false spots in each bin. For this study, $n = 2$ was chosen, as statistically there is a <3% chance that the number of false spots in each bin exceeds $R_i^{\mu} + 2R_i^{\mathrm{SD}}$. The total number of real spots was reported as 'SR counts', which was calculated by summing C_i^{μ} for every bin of the test sample 2D histogram. The limit of detection (LOD) was calculated using the following formula (*65*): LOD = SR $\text{counts}_{\text{control}} + 1.645 \times \text{SD}_{\text{control}} + 1.645 \times \text{SD}_{\text{min}}$, where SD_{min} is the lowest protein concentration in which the mean number of SR counts exceeds its standard deviation. Note that with shape analysis, the probability that a sample would have SR counts ≥1 by chance alone is <3%. To further reduce the false positive rate for circulating mutant protein detection in clinical samples, we only considered samples to be positive at SR counts >3.

Analysis of protein aggregation

Various GFP-fused mutant p53 ($p53^{R175}$, $p53^{L344P}$) or wildtype p53 were expressed in a p53-deficient cell line, BHK21. The concentrations of p53 in the cell lysates were normalized by on denaturing SDS-PAGE. Serial dilutions were performed based on these normalized concentrations. Individual fluorescent spots were initially selected on the first imaging frame using ThunderSTORM for the various p53 protein conformational variants at different concentrations. Because the conformational variants produce spots with distinct intensity distributions, intensity histograms were generated from these spots, and fixed Gaussian fitting was applied to identify curves for different structural populations of p53 (e.g., monomer, dimer, tetramer, octamer). The areas under the curve for populations greater than or equal to tetramer were integrated and defined as aggregates. The structural compositions of p53 in each sample were hence determined based on the relationship between percentage of aggregates and spot number. Note that although spot number is directly influenced by protein concentration, the relationship between protein concentration and spot number varies depending on p53 conformation (for example, monomers yield a larger number of imaging spots than aggregates for any given total p53 protein concentration). The spread of intensity distributions allowed us to distinguish among the different p53 variants; mutant $p53^{R175H}$ aggregates had a wider dispersion of fluorescent spot intensities compared to wildtype p53, which likewise had a wider dispersion than mutant $p53^{L344P}$ monomers. We quantified the dispersion of these intensity distributions using the Fano factor, defined as the variance in intensity of an image divided by the mean intensity. The Fano factor serves as an index of aggregation status. For instance, $p53^{R175H}$ complexes showed a higher Fano factor than $p53^{L344P}$ monomers. There was a linear relationship between Fano factor and spot number for all p53 conformational variants, each with distinct slopes. Therefore, by plotting standard curves for Fano factor versus spot number for each of the conformational variants, the aggregation status of p53 could be determined.

Single-molecule anti-p53 autoantibody detection

Recombinant human p53 protein was biotinylated with EZ-Link Sulfo-NHS-Biotin reagent and purified by gel filtration chromatography on 7 kD columns as described above. Biotinylated protein was stored at -20°C in PBS containing 20% glycerol and 0.1% sodium azide. The purified biotinylated protein was coated in one channel of a dual-channel single-molecule microfluidic capture chip via a streptavidin linker (Thermo Fisher Scientific); the other channel was kept uncoated as a background control. Streptavidin was used instead of NeutrAvidin (a deglycosylated

form of avidin protein found in chicken egg white) since most individuals had large amounts of circulating anti-NeutrAvidin IgG, probably because these people eat eggs. Human plasma samples were diluted 10^3-10^6× in $SMAC^{BSA}$ buffer and passed continuously through both channels of the SMAC chip for 2 hr by oscillating flow. The chip was then washed with $SMAC^{BSA}$ buffer (1 ml) and incubated with Alexa Fluor 488-labeled goat anti-human IgG (1-10 nM) for 30 min. The chip was washed again and visualized by TIRF microscopy. The spots in the uncoated channel reflected the amount of basal human IgG deposited on the chip via non-specific binding. Autoantibody levels were hence calculated by subtracting this number of non-specific IgG counts from total counts in the p53-coated channel.

qPCR

Serum DNA was extracted with the Plasma/Serum Cell-Free Circulating DNA Purification Micro Kit (Norgen Biotek) according to manufacturer instructions. Briefly, 50 µl of mouse serum was collected and eluted with nuclease-free water (50 µl). The eluate (2 µl) was then used for PCR amplification with 2× SsoFast EvaGreen Supermix (Bio-Rad) (10 µl), 5 µM GFP primer mix (2 µl), and nuclease-free water (6 µl) on a CFX96 qPCR system (Bio-Rad) with the following thermal cycling conditions: 98°C for 1 min followed by 60 cycles of 98°C for 5 sec and 60°C for 10 sec. A melt curve was performed from 65°C to 95°C. To generate qPCR standard curves for *gfp* and *p53*, *gfp* and *hp53* plasmid DNA (2 pg), respectively, were serially diluted. Standard curves displayed cycle threshold (C_t) values as a function of DNA copy number. Primer pairs for p53 qPCR were: 5' CCTTGCCGTCCCAAGCA 3' (forward) and 5' GTGTAGGAGCTGCTGGTG 3' (reverse). Primer pairs for GFP qPCR were: 5' ACGTAAACGGCCACAAGTTC 3' (forward) and 5' AAGTCGTGCTGCTTCATGTG 3' (reverse).

p53 native protein gel electrophoresis

BHK21 cells were transfected using Lipofectamine 2000 with mutant or wildtype p53 constructs (0.1-20 µg DNA) in 6-well plates. After 16 hr, lysate was prepared as described above with 18 mM CHAPS in TBS containing DNase and protease inhibitor. Lysate was added with 20% glycerol and 5 mM Coomassie G-250 dye then loaded onto a 3-12% native PAGE Bis-Tris gel (Invitrogen). Electrophoresis was performed in 50 mM Bis-Tris and 50 mM Tricine plus 0.02% Coomassie G-250 dye in the cathode buffer for 2 hr at 100 V. Proteins were transferred to a polyvinylidene membrane and stained with Coomassie G-250 dye. The membrane was fixed with 8% acetic acid for 20 min and destained with 100% methanol. p53 proteins were detected by immunoblot with DO-1 antibodies and HRP-conjugated anti-mouse secondary antibodies.

References:

1. D. A. Giljohann, C. A. Mirkin, Drivers of biodiagnostic development. *Nature* **462**, 461-464 (2009).
2. J. M. Barletta, D. C. Edelman, N. T. Constantine, Lowering the detection limits of HIV-1 viral load using real-time immuno-PCR for HIV-1 p24 antigen. *Am J Clin Pathol* **122**, 20-27 (2004).
3. P. R. Srinivas, B. S. Kramer, S. Srivastava, Trends in biomarker research for cancer detection. *Lancet Oncol* **2**, 698-704 (2001).
4. D. M. Rissin *et al.*, Single-molecule enzyme-linked immunosorbent assay detects serum proteins at subfemtomolar concentrations. *Nat Biotechnol* **28**, 595-599 (2010).
5. J. M. Nam, C. S. Thaxton, C. A. Mirkin, Nanoparticle-based bio-bar codes for the ultrasensitive detection of proteins. *Science* **301**, 1884-1886 (2003).
6. S. Fredriksson *et al.*, Multiplexed protein detection by proximity ligation for cancer biomarker validation. *Nat Methods* **4**, 327-329 (2007).
7. S. Fredriksson *et al.*, Protein detection using proximity-dependent DNA ligation assays. *Nat Biotechnol* **20**, 473-477 (2002).
8. V. Ruzicka, W. Marz, A. Russ, W. Gross, Immuno-PCR with a commercially available avidin system. *Science* **260**, 698-699 (1993).
9. T. Sano, C. L. Smith, C. R. Cantor, Immuno-PCR: very sensitive antigen detection by means of specific antibody-DNA conjugates. *Science* **258**, 120-122 (1992).
10. S. Shashkova, M. C. Leake, Single-molecule fluorescence microscopy review: shedding new light on old problems. *Biosci Rep* **37**, (2017).
11. A. Jain *et al.*, Probing cellular protein complexes using single-molecule pull-down. *Nature* **473**, 484-488 (2011).
12. A. Jain, R. Liu, Y. K. Xiang, T. Ha, Single-molecule pull-down for studying protein interactions. *Nat Protoc* **7**, 445-452 (2012).
13. P. T. Charles *et al.*, Reduction of Non-Specific Protein Adsorption Using Poly(ethylene) Glycol (PEG) Modified Polyacrylate Hydrogels In Immunoassays for Staphylococcal Enterotoxin B Detection. *Sensors (Basel)* **9**, 645-655 (2009).
14. A. D. Stroock *et al.*, Chaotic mixer for microchannels. *Science* **295**, 647-651 (2002).
15. M. S. Litwin, H. J. Tan, The Diagnosis and Treatment of Prostate Cancer: A Review. *JAMA* **317**, 2532-2542 (2017).
16. F. H. Schroder *et al.*, Screening and prostate cancer mortality: results of the European Randomised Study of Screening for Prostate Cancer (ERSPC) at 13 years of follow-up. *Lancet* **384**, 2027-2035 (2014).
17. F. H. Schroder *et al.*, Screening and prostate-cancer mortality in a randomized European study. *N Engl J Med* **360**, 1320-1328 (2009).
18. H. Lilja, D. Ulmert, A. J. Vickers, Prostate-specific antigen and prostate cancer: prediction, detection and monitoring. *Nat Rev Cancer* **8**, 268-278 (2008).
19. E. M. Genega, B. Hutchinson, V. E. Reuter, P. B. Gaudin, Immunophenotype of high-grade prostatic adenocarcinoma and urothelial carcinoma. *Mod Pathol* **13**, 1186-1191 (2000).
20. F. H. Schroder *et al.*, Prostate cancer detection at low prostate specific antigen. *J Urol* **163**, 806-812 (2000).

21. M. H. Sokoloff, X. J. Yang, M. Fumo, D. Mhoon, C. B. Brendler, Characterizing prostatic adenocarcinomas in men with a serum prostate specific antigen level of < 4.0 ng/mL. *BJU Int* **93**, 499-502 (2004).
22. B. A. Mahal, A. A. Aizer, J. A. Efstathiou, P. L. Nguyen, Association of very low prostate-specific antigen levels with increased cancer-specific death in men with high-grade prostate cancer. *Cancer* **122**, 78-83 (2016).
23. T. Okazaki, S. Chikuma, Y. Iwai, S. Fagarasan, T. Honjo, A rheostat for immune responses: the unique properties of PD-1 and their advantages for clinical application. *Nat Immunol* **14**, 1212-1218 (2013).
24. S. H. Baumeister, G. J. Freeman, G. Dranoff, A. H. Sharpe, Coinhibitory Pathways in Immunotherapy for Cancer. *Annu Rev Immunol* **34**, 539-573 (2016).
25. D. M. Pardoll, The blockade of immune checkpoints in cancer immunotherapy. *Nat Rev Cancer* **12**, 252-264 (2012).
26. K. E. Brown, G. J. Freeman, E. J. Wherry, A. H. Sharpe, Role of PD-1 in regulating acute infections. *Curr Opin Immunol* **22**, 397-401 (2010).
27. G. Chen *et al.*, Exosomal PD-L1 contributes to immunosuppression and is associated with anti-PD-1 response. *Nature* **560**, 382-386 (2018).
28. J. Zhou *et al.*, Soluble PD-L1 as a Biomarker in Malignant Melanoma Treated with Checkpoint Blockade. *Cancer Immunol Res* **5**, 480-492 (2017).
29. D. Gardiner *et al.*, A randomized, double-blind, placebo-controlled assessment of BMS-936558, a fully human monoclonal antibody to programmed death-1 (PD-1), in patients with chronic hepatitis C virus infection. *PLoS One* **8**, e63818 (2013).
30. J. R. Brahmer *et al.*, Safety and activity of anti-PD-L1 antibody in patients with advanced cancer. *N Engl J Med* **366**, 2455-2465 (2012).
31. S. L. Topalian *et al.*, Safety, activity, and immune correlates of anti-PD-1 antibody in cancer. *N Engl J Med* **366**, 2443-2454 (2012).
32. M. Nishino, N. H. Ramaiya, H. Hatabu, F. S. Hodi, Monitoring immune-checkpoint blockade: response evaluation and biomarker development. *Nat Rev Clin Oncol* **14**, 655-668 (2017).
33. R. Roden, T. C. Wu, How will HPV vaccines affect cervical cancer? *Nat Rev Cancer* **6**, 753-763 (2006).
34. W. Zou, L. Chen, Inhibitory B7-family molecules in the tumour microenvironment. *Nat Rev Immunol* **8**, 467-477 (2008).
35. O. Saglam, J. Conejo-Garcia, PD-1/PD-L1 immune checkpoint inhibitors in advanced cervical cancer. *Integr Cancer Sci Ther* **5**, (2018).
36. O. L. Reddy, P. I. Shintaku, N. A. Moatamed, Programmed death-ligand 1 (PD-L1) is expressed in a significant number of the uterine cervical carcinomas. *Diagn Pathol* **12**, 45 (2017).
37. M. Polanski, N. L. Anderson, A list of candidate cancer biomarkers for targeted proteomics. *Biomark Insights* **1**, 1-48 (2007).
38. E. P. Diamandis, The failure of protein cancer biomarkers to reach the clinic: why, and what can be done to address the problem? *BMC Med* **10**, 87 (2012).
39. S. H. Lee *et al.*, p53, secreted by K-Ras-Snail pathway, is endocytosed by K-Ras-mutated cells; implication of target-specific drug delivery and early diagnostic marker. *Oncogene* **28**, 2005-2014 (2009).

40. Q. Wang *et al.*, Mutant proteins as cancer-specific biomarkers. *Proc Natl Acad Sci U S A* **108**, 2444-2449 (2011).
41. K. Y. Lin *et al.*, Treatment of established tumors with a novel vaccine that enhances major histocompatibility class II presentation of tumor antigen. *Cancer Res* **56**, 21-26 (1996).
42. C. M. Carlson, J. L. Frandsen, N. Kirchhof, R. S. McIvor, D. A. Largaespada, Somatic integration of an oncogene-harboring Sleeping Beauty transposon models liver tumor development in the mouse. *P Natl Acad Sci USA* **102**, 17059-17064 (2005).
43. M. Ignatiadis, G. W. Sledge, S. S. Jeffrey, Liquid biopsy enters the clinic - implementation issues and future challenges. *Nat Rev Clin Oncol* **18**, 297-312 (2021).
44. A. M. Lennon *et al.*, Feasibility of blood testing combined with PET-CT to screen for cancer and guide intervention. *Science* **369**, (2020).
45. J. D. Cohen *et al.*, Detection and localization of surgically resectable cancers with a multi-analyte blood test. *Science*, (2018).
46. A. Bardelli, K. Pantel, Liquid Biopsies, What We Do Not Know (Yet). *Cancer cell* **31**, 172-179 (2017).
47. J. D. Cohen *et al.*, Combined circulating tumor DNA and protein biomarker-based liquid biopsy for the earlier detection of pancreatic cancers. *Proc Natl Acad Sci U S A* **114**, 10202-10207 (2017).
48. C. Bettegowda *et al.*, Detection of circulating tumor DNA in early- and late-stage human malignancies. *Sci Transl Med* **6**, 224ra224 (2014).
49. T. J. Sweeney *et al.*, Visualizing the kinetics of tumor-cell clearance in living animals. *Proc Natl Acad Sci U S A* **96**, 12044-12049 (1999).
50. A. J. Levine, M. Oren, The first 30 years of p53: growing ever more complex. *Nat Rev Cancer* **9**, 749-758 (2009).
51. P. A. Muller, K. H. Vousden, p53 mutations in cancer. *Nature cell biology* **15**, 2-8 (2013).
52. P. A. Muller, K. H. Vousden, Mutant p53 in cancer: new functions and therapeutic opportunities. *Cancer cell* **25**, 304-317 (2014).
53. N. Cancer Genome Atlas Research, Integrated genomic analyses of ovarian carcinoma. *Nature* **474**, 609-615 (2011).
54. T. Soussi, p53 Antibodies in the sera of patients with various types of cancer: a review. *Cancer Res* **60**, 1777-1788 (2000).
55. R. T. Fortner *et al.*, Ovarian cancer early detection by circulating CA125 in the context of anti-CA125 autoantibody levels: Results from the EPIC cohort. *Int J Cancer* **142**, 1355-1360 (2018).
56. A. E. Lokshin *et al.*, Circulating IL-8 and anti-IL-8 autoantibody in patients with ovarian cancer. *Gynecol Oncol* **102**, 244-251 (2006).
57. L. A. Torre *et al.*, Ovarian cancer statistics, 2018. *CA Cancer J Clin* **68**, 284-296 (2018).
58. G. Wang, A. R. Fersht, Multisite aggregation of p53 and implications for drug rescue. *Proc Natl Acad Sci U S A* **114**, E2634-E2643 (2017).
59. J. F. Kerr, A. H. Wyllie, A. R. Currie, Apoptosis: a basic biological phenomenon with wide-ranging implications in tissue kinetics. *Br J Cancer* **26**, 239-257 (1972).
60. S. Sperandio, I. de Belle, D. E. Bredesen, An alternative, nonapoptotic form of programmed cell death. *Proc Natl Acad Sci U S A* **97**, 14376-14381 (2000).

61. L. M. Schwartz, S. W. Smith, M. E. Jones, B. A. Osborne, Do all programmed cell deaths occur via apoptosis? *Proc Natl Acad Sci U S A* **90**, 980-984 (1993).
62. J. Debnath, E. H. Baehrecke, G. Kroemer, Does autophagy contribute to cell death? *Autophagy* **1**, 66-74 (2005).
63. D. Gozuacik, A. Kimchi, Autophagy as a cell death and tumor suppressor mechanism. *Oncogene* **23**, 2891-2906 (2004).
64. M. Ovesny, P. Krizek, J. Borkovec, Z. Svindrych, G. M. Hagen, ThunderSTORM: a comprehensive ImageJ plug-in for PALM and STORM data analysis and super-resolution imaging. *Bioinformatics* **30**, 2389-2390 (2014).
65. D. A. Armbruster, T. Pry, Limit of blank, limit of detection and limit of quantitation. *Clin Biochem Rev* **29 Suppl 1**, S49-52 (2008).

Acknowledgments: We are grateful to Dr. Christopher Bohrer and Mr. Huy Vo for assistance with microfluidic device design and fabrication. We thank Dr. TC Wu (T.C.W.) and Dr. Bert Vogelstein for their insightful input on the manuscript. We also thank Dr. Xinxing Yang, Dr. Ryan McQuillen, and Dr. Kelsey Bettridge for helpful discussion; **Funding:** This work was supported by NIH and National Cancer Institute (NIH/NCI) grants 2 P50 CA098252-06, NIH/NCI 2 P50 CA96784-06, NIH/NCI 1 R01 CA114425-06, and NIH/NCI 1 R21 CA194896-01 to C.F.H., as well as Johns Hopkins University Discovery Awards and the Hamilton Innovation Award to J.X. C.P.M. was a recipient of the Ruth L. Kirschstein National Research Service Award (NIH F30 CA177221) and NIH Medical Scientist Training Program Award. S.C.W. was a recipient of a Taiwanese Government Scholarship; **Author contributions:** C.P.M., S.C.W., and C.F.H. designed research; C.P.M., S.C.W., and Y.P.S. conducted single-molecule imaging experiments and data processing. Y.P.S. and S.H.T. performed mouse experiments and ELISA. L.H., A.A.W. conducted protein purification; R.B.S.R. supplied human plasma samples; C.P.M., S.C.W., R.B.S.R., J.X. and C.F.H. wrote the paper; **Competing interests:** C.P.M., S.C.W., T.C.W., J.X., and C.F.H. are inventors of two patents covering the SMAC platform, as well as the data analysis algorithms submitted to the U.S. Patent Office; and **Data and materials availability:** Key data to support the conclusions of this study are available in the main figures and Supplementary Materials. Additional substantiating data, including raw data for all figures, are available upon request. Programming codes for the SMAC analysis algorithms are available upon request. Correspondence and requests for materials should be addressed to chung2@jhmi.edu.

Supplementary Materials:

Figures S1-S15

Tables S1-S5

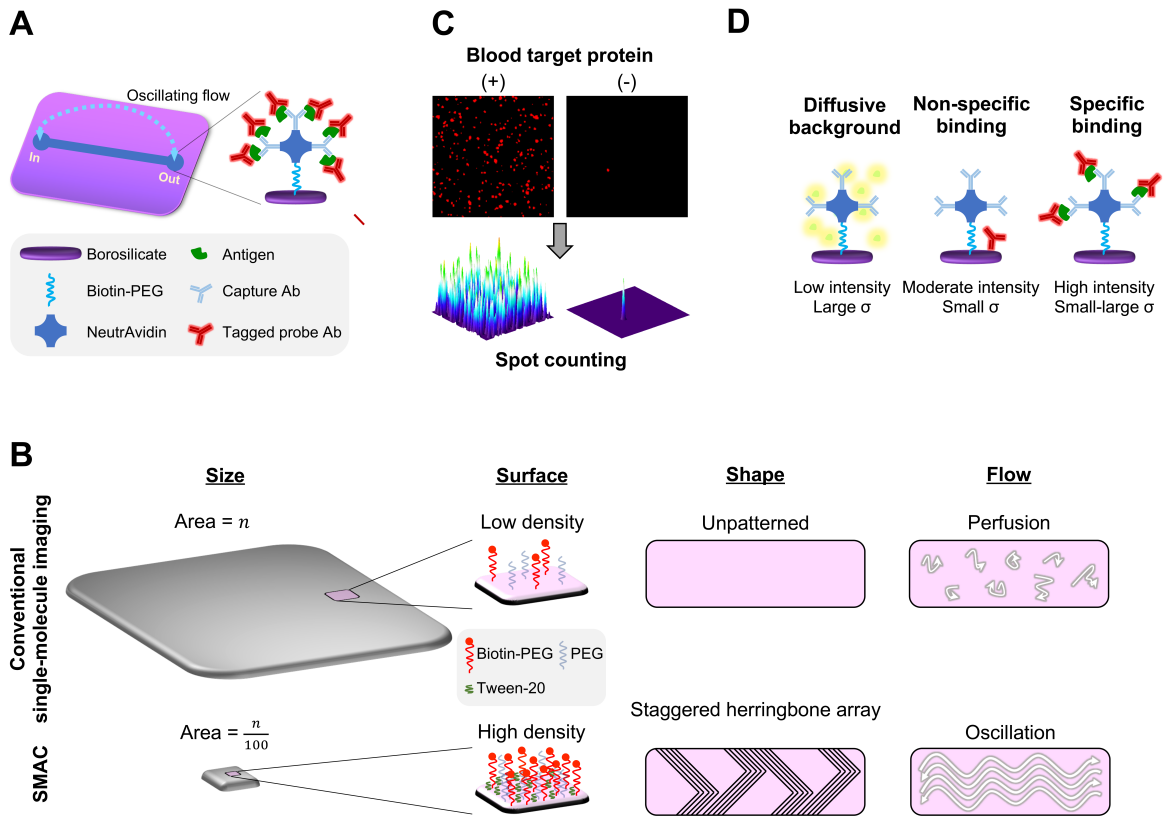

Fig. 1. SMAC chip design. (**A**) Schematic diagram of the SMAC platform. Proteins-of-interest were pulled down as clusters via continuous oscillating flow on a multivalent microfluidic device and then probed with fluorophore-labeled detection antibody. (**B**) Schematic diagram depicting features of SMAC (bottom), contrasted to conventional single-molecule imaging methods (top), that enable single-molecule imaging of blood samples at sub-femtomolar sensitivity. The miniature size, high-density capture surface, patterned channel shape, and continuous oscillating flow scheme of the SMAC chip synergize to efficiently concentrate proteins-of-interest on the chip. (**C**) Target protein clusters were visualized by TIRF microscopy. (**D**) Schematic diagrams depicting different binding types that give rise to different fluorescence intensity and spot size combinations. Scale bar, 4 μm.

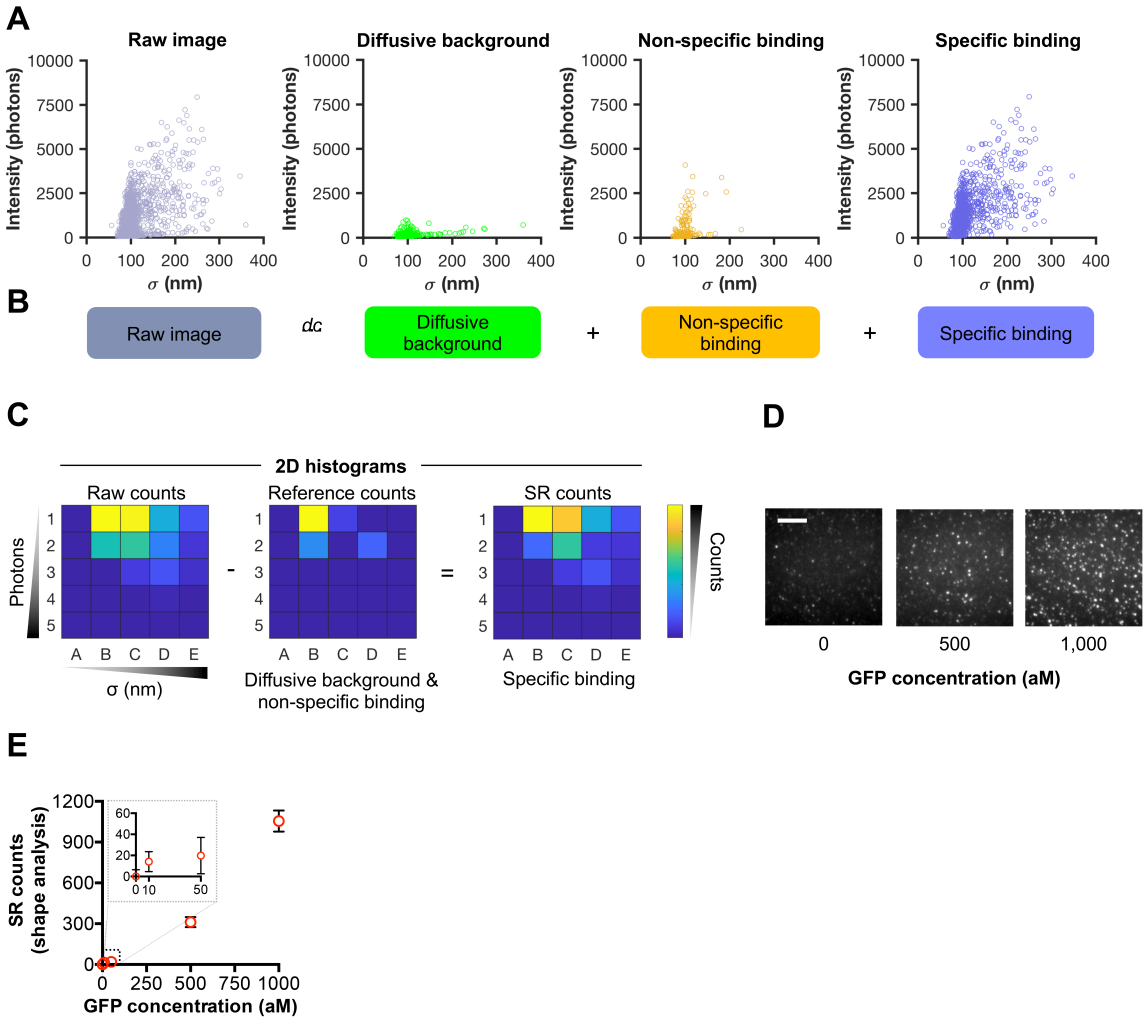

Fig. 2. SMAC and protein analysis methods. (**A**) Schematic diagrams depicting different binding types that give rise to different fluorescence intensity and spot size combinations. Scatter plots (**A**) and decomposition (**B**) of spot sizes (σ) and intensities arising from different binding types after Gaussian fitting of each spot. These data were converted into a two-dimensional (2D) histogram of intensity and σ as shown in (**C**). (**C**) The number of specific binding spots (SR counts) is obtained by subtracting the 2D histogram of a scaled reference histogram conveying the intensity-σ distributions of diffusive background and non-specific binding from the 2D histogram of raw counts (see Methods for details). (**D**) Representative SMAC images of purified GFP molecules at 500 aM and 1 fM concentrations. The intrinsic fluorescence of GFP was measured without detection antibody. (**E**) Graph illustrating the sensitivity of SMAC with shape analysis (SR counts) using purified GFP from 10 aM to 1 fM. Data are expressed as mean ± SD. Scale bar, 4 μm.

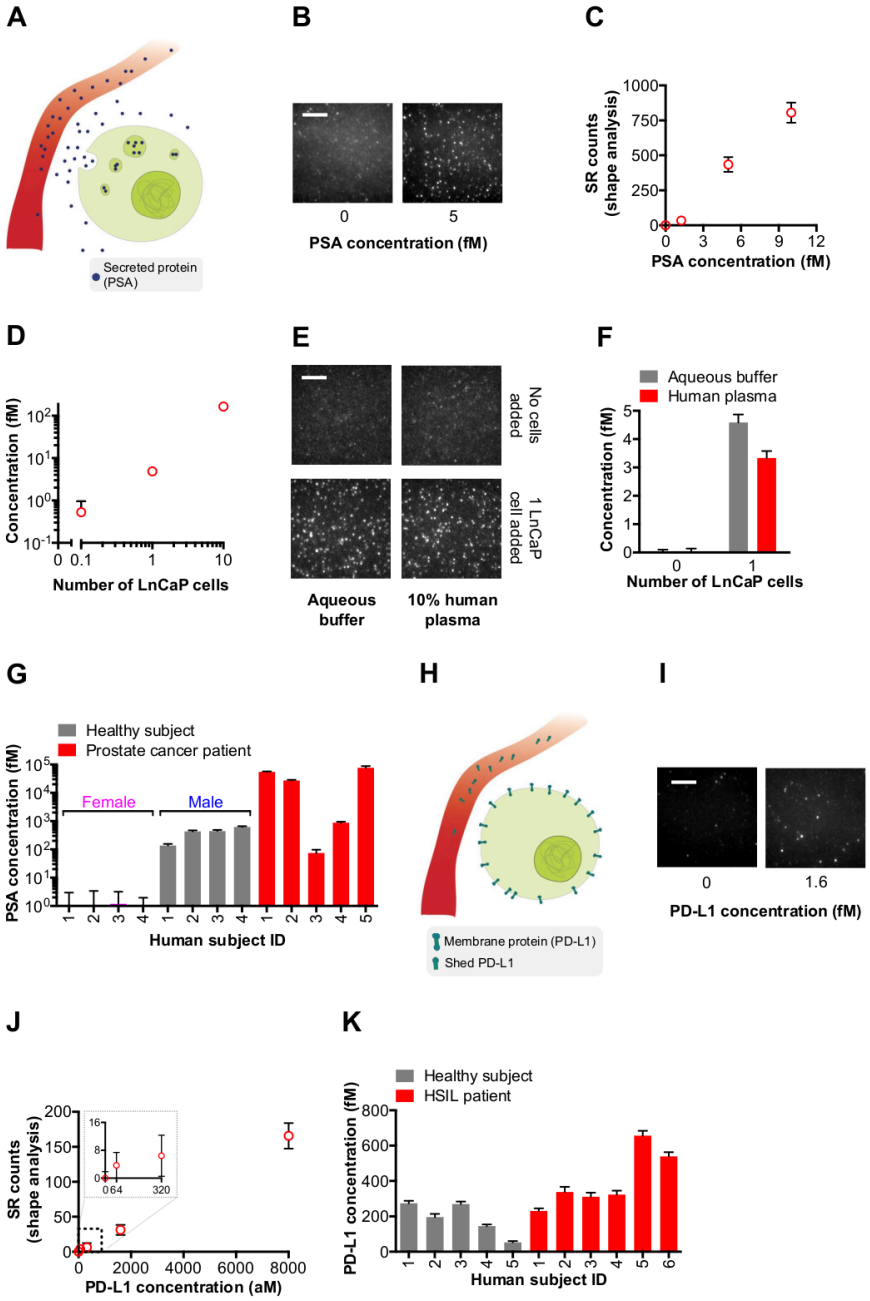

Fig. 3. Detection of secreted and membrane proteins in blood by single-molecule imaging. (A) Schematic diagram of secreted PSA release from a tumor cell (lime) into a blood vessel (red). SMAC images (**B**) and shape analysis (**C**) of purified human PSA at fM concentrations in aqueous buffer. (**D**) Quantification of PSA in lysate from different numbers of human prostate cancer cells (LnCaP) added into aqueous buffer. SMAC images (**E**) and quantification of PSA (**F**) in lysate from one LnCaP cell in either aqueous buffer or human plasma. (**G**) PSA levels in the blood of prostate cancer patients (n = 5) and healthy male (n = 4) and female (n = 4) control blood donors.

(**H**) Schematic diagram of membrane-bound PD-L1 release from a tumor cell (lime) into a blood vessel (red). SMAC images (**I**) and shape analysis (**J**) of purified human PD-L1 at fM concentrations in aqueous buffer. (**K**) Quantification of circulating PD-L1 levels in patients with high-grade squamous intraepithelial lesions (HSIL; $n = 6$) and healthy donors ($n = 5$). PSA data and PD-L1 data are expressed as mean ± SD. Scale bars, 4 μm.

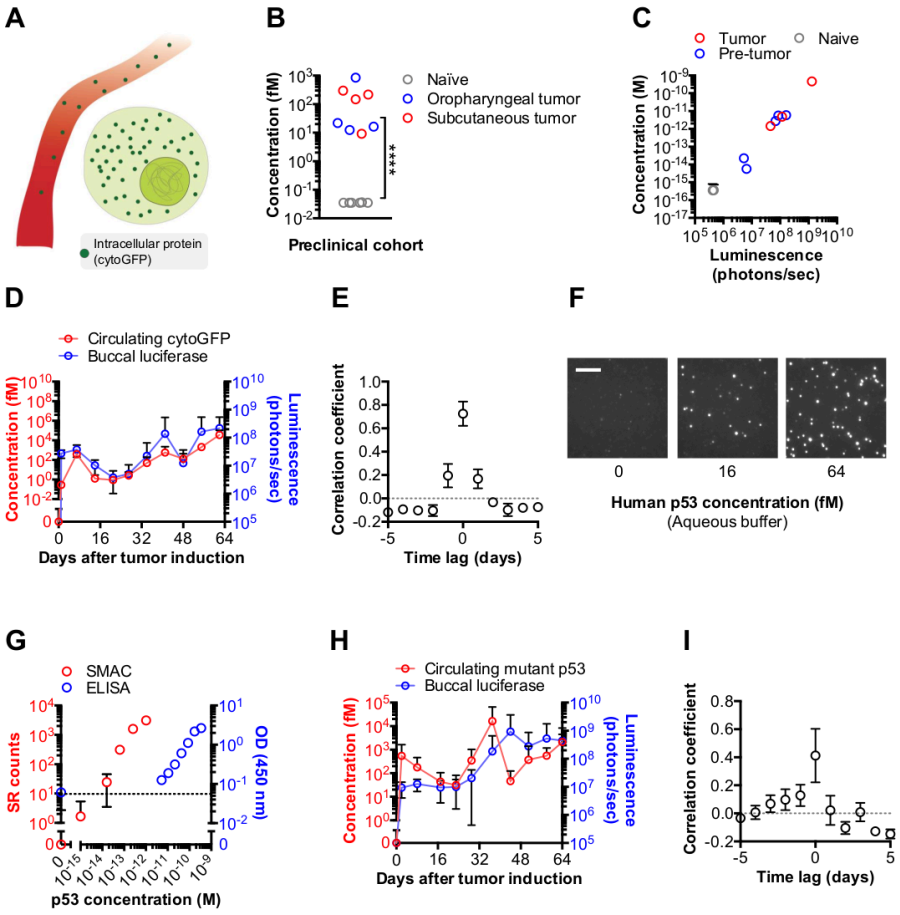

Fig. 4. Detection of cytoplasmic and nuclear proteins in blood by single-molecule imaging. (**A**) Schematic diagram of intracellular cytoGFP release from a tumor cell (lime) into a blood vessel (red). (**B**) SMAC quantification of serum cytoGFP levels in naïve mice (gray circles; $n = 8$) as well as tumor-bearing mice one week after oropharyngeal (blue circles; $n = 4$) or subcutaneous (red circles; $n = 4$) injection of cytoGFP$^+$ tumor cells (TC-1). (**C-E**) To induce a spontaneous cytoGFP$^+$ tumor, mice ($n = 10$) were administered with DNA encoding Ras^{G12V}, p53 shRNA, cytoGFP, and luciferase. Graph depicting the relationship between tumor luciferase and serum cytoGFP concentrations assessed by SMAC at an endpoint of more than two months (**C**) or throughout the first two months (**D**). In (**C**), tumor-induced mice that displayed a grossly visible tumor were labeled 'tumor' (red circles), while those that did not were labeled 'pre-tumor' (blue circles). Using the kinetics data in (**D**), the time correspondence between serum cytoGFP levels and tumor burden was determined by cross-correlation analysis (**E**). (**F**) SMAC images of purified human p53 at fM concentrations in aqueous buffer. (**G**) Comparison of the sensitivity of SMAC with shape analysis (SR counts, red circles) and ELISA ($OD_{450\ nm}$, blue circles) using purified human p53. The dotted line indicates the ELISA detection limit. (**H**, **I**) To stimulate a spontaneous tumor carrying mutant human p53, mice ($n = 10$) were administered with DNA encoding human p53^{R175H}, Ras^{G12V}, and luciferase. Time course (**H**) and cross-correlation (**I**) plots depicting the relationship between tumor luciferase and serum mutant p53 levels measured by SMAC. For cross-

correlation plots, each unit time lag is around five days. All data are expressed as mean ± SD. ****$P<0.0001$. P-values are from a two-sided unpaired t-test. Scale bar, 4 μm.

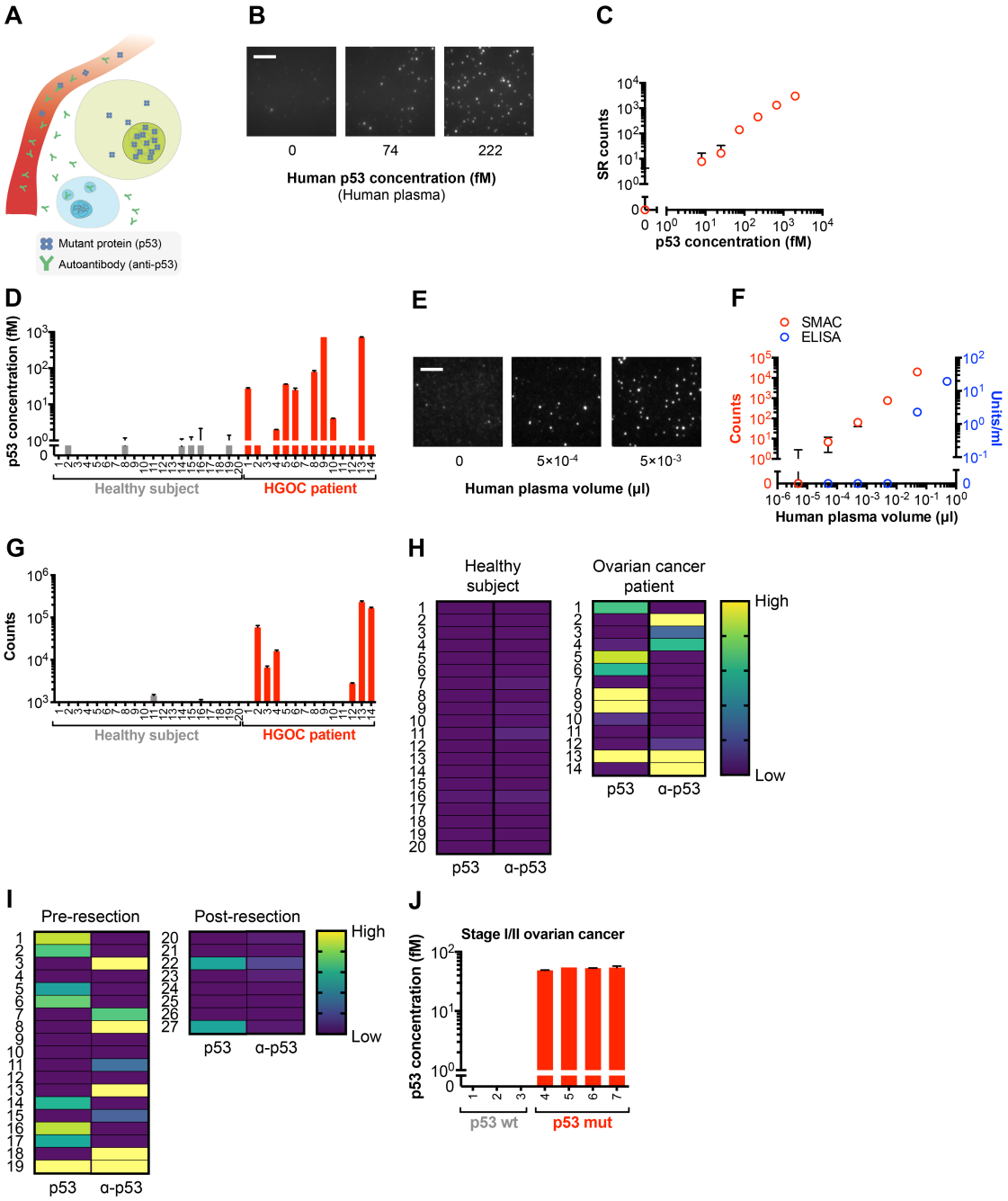

Fig. 5. Detection of circulating mutant proteins and autoantibodies in blood by single-molecule imaging. (**A**) Schematic diagram depicting release of nuclear p53 from a tumor cell (lime) and anti-p53 autoantibodies from a tumor-specific B cell (aqua) into a blood vessel (red). SMAC images (**B**) and shape analysis (**C**) of purified human p53 added at fM concentrations in human plasma. (**D**) Shape analysis of circulating mutant p53 levels in plasma from high-grade ovarian cancer (HGOC) patients and healthy female blood donors. (**E**) SMAC images of endogenous anti-p53 autoantibodies in different plasma volumes, from the microliter (µl; 10^{-6} l) to picoliter (pl; 10^{-12} l) range, in an HGOC patient. (**F**) Comparison of the sensitivity of SMAC

(counts, red circles) and ELISA (units/ml, blue circles) using human anti-p53 autoantibodies in human plasma. (**G**) Quantification of endogenous plasma anti-p53 autoantibodies from HGOC patients and healthy female blood donors; same cohort as in (**D**). (**H**) Heat map depicting the relative levels of circulating mutant p53 or anti-p53 autoantibodies in the blood of HGOC patients and healthy blood donors; same cohort as in (**D**) and (**G**). (**I**) Heat map depicting the relative levels of circulating mutant p53 or anti-p53 autoantibodies in an independent cohort of FIGO stage III ovarian cancer patients with p53-mutant tumors either before or after surgical resection. (**J**) SMAC analysis of circulating mutant p53 levels in early-stage (FIGO stage I/II) ovarian cancer patients with either p53-wildtype or p53-mutant tumors. Data for individual human plasma samples (**D**, **G**, **J**) are expressed as mean ± SE; all other data are expressed as mean ± SD. Scale bars, 4 μm.